SIMULATION OF IMPULSIVE WAVE ACTION ON SUBMERGED HORIZONTAL PLATE USING A WATER-AIR TWO-PHASE FLUIDS NUMERICAL MODEL

Xiao Shi [1], Qin Jiang[1,2], Jie Hao[1]

Impulsive wave force on marine structures is a vital hydrodynamic parameter for the design of coastal and offshore structures. In this study, an improved numerical wave model dealing with compressible-incompressible air water two-phase fluids is applied for the wave-structure interaction problems involving impulsive wave actions. The fifth-order accurate weighted essentially non-oscillation (WENO) scheme is used to solve the Navier-Stokes equation for fluid flows, and the improved multi-dimensional tangent of hyperbola for interface capturing scheme with weighted line interface calculation method (THINC/WLIC) is adopted to track the interface. By comparing the numerical results with analytical solutions and experimental data, the accuracy of the present numerical wave model is validated. Subsequently, the model is applied to simulate the impact process of regular waves on a submerged horizontal plate. A comparison between the simulation results and experimental data demonstrates that the present numerical model provides high-precision predictions of the impact pressure. By analyzing the wave impact process on the plate under different relative wavelength conditions, the effect of the number and distribution of air pockets on the pressure distribution at the bottom of the plate is investigated.

Keywords: water-gas two-phase flow ; wave impact; gas compressibility; numerical wave model; horizontal plate

1.INTRODUCTION

One of the dominant hydrodynamic factors that may cause the failure of marine structures is the impact of wave forces. As exploration extends further into deep-sea, maritime engineering is advancing towards the development of larger, lighter, and deeper structures. Flat plates, commonly employed in offshore platforms, such as decks, ships, and coastal defenses, are thus vulnerable to increasingly harsh marine conditions and severe wave impacts. During wave impact events, breaking waves generate substantial forces that act upon maritime infrastructure, potentially resulting in localized or even total structural failure. Therefore, accurately assessing impact pressures is crucial in the design of structures.

A lot of experimental and numerical research has been conducted on wave impact loads on deck structures. Ren and Wang (2004) performed numerical simulations of random wave impacts on ship superstructures based on the Reynolds-averaged equations, conducting a parametric study on different incident waves, air clearance levels and structural sizes. Ma et al. (2019) carried out both numerical simulations and scale model experiments on wave impact loads on inclined plates with various tilt angles, systematically investigating the influence of three key wave parameters on impact load: relative deck width, relative wave height, and plate tilt angle. Ma and Swan (2020) conducted experimental studies on deck structure wave loads under extreme wave conditions, examining the relative importance of various incident wave characteristics. Their research showed that the applied loads mainly depend on the wave shape and the motion of the water particles at the crest, both of which are strongly influenced by wave breaking. Duong et al. (2021) performed a set of experiments in a two-dimensional wave tank, studying the velocity distribution, vertical force, and pressure distribution at the bottom of the deck under different deck clearances and focused waves with varying wave crest heights.

When waves impact on a flat plate, a substantial volume of air may be entrained into the wave. Due to the large contact area of the surface structure, the gas is unable to escape promptly, often resulting in the formation of a confined space. Under such circumstances, the role of air in wave impact on the structure cannot be disregarded (Chang et al., 2011; Ryu et al., 2007, 2005). During violent wave impact on structures, the presence of entrapped air significantly influences the impact loading(Bullock et al., 2007; Liu et al., 2019; Sun et al., 2019). Zhai et al. (2021) conducted a series of experiments to study the spatial and instantaneous distribution of impact pressures generated by regular waves on flat plates and flat plates with four vertical columns. They further analyzed the effect of air compressibility on impact forces using both compressible and incompressible flow solvers. The results indicated significant variations in both pressure distribution and the magnitude of impact pressures for the two types of deck configurations. Therefore, the compressibility of air should not be ignored in the study of wave impact on plate.

Due to scale effects, the influence of air compressibility on impact pressure measured in most experiments is minimal, making it difficult to reproduce real-world physical phenomena. With the increasing computational power of modern computers, Computational Fluid Dynamics (CFD) has rapidly advanced. Along with physical experiments and theoretical analysis, numerical simulation has become one of the three primary research methods for studying fluid-structure interactions (Ghalandari

[1] Hohai University, College of Harbour, Coastal and Offshore Engineering, P.R. China
[2] Corresponding author, qjiang@hhu.edu.cn

et al., 2019; Salih et al., 2019). Numerical models not only overcome scale effects inherent in physical modeling, but also offer advantages such as improved cost-effectiveness and flexibility, making them highly promising for future applications. In recent years, significant progress has been made in the development of incompressible two-phase flow models based on the incompressible Navier-Stokes equations (Zhao et al., 2010; E. et al., 2014; Hu et al., 2016). However, due to the complexity of wave impact problems, most wave numerical models still neglect the compressibility of gas. Yabe et al. (1991; 2001) proposed a set of governing equations for two-phase water-air flow, where the water phase is weakly compressible and the air phase is compressible. However, these equations suffers from issues such as the use of weak compressibility for the water phase and density diffusion at the water-air interface. Wei et al. (2021) developed a simplified set of equations with an incompressible water phase and compressible air phase based on Yabe et al.'s equations, which not only maintains a reasonable level of simulation accuracy but also significantly enhances computational efficiency.

This study develops a wave numerical simulation model for compressible gas and incompressible water phases, based on the improved two-phase water-air flow governing equations proposed by Wei et al. (2021). The model is used to simulate the wave impact process on a horizontal plate in order to analyze the effect of air on the pressure distribution relative to the plate's bottom. Section 2 presents the compressible and incompressible air-water numerical model with a momentum wave maker. In Section 3, In Section 3, regular waves are generated and compared with the analytical solution. Section 4 describes the wave impact process on a horizontal plate. Finally, some conclusions are given in the last section.

2.NUMERICAL IMPLEMENTATION

2.1Governing equations

Yabe et al. (1991) proposed a general solution method for both compressible and incompressible single-phase flow dynamics. The governing equations are presented as follows:

$$\frac{\partial \rho}{\partial t}+u_i\frac{\partial \rho}{\partial x_i}=-\rho\frac{\partial u_i}{\partial x_i} \tag{1a}$$

$$\frac{\partial u_i}{\partial t}+u_j\frac{\partial u_i}{\partial x_i}=-\frac{1}{\rho}\frac{\partial p}{\partial x_i} \tag{1b}$$

$$\frac{\partial p}{\partial t}+u_i\frac{\partial p}{\partial x_i}=-\gamma p\frac{\partial u_i}{\partial x_i} \tag{1c}$$

where, ρ is the density, u_i is the velocity, p is the pressure, and γ is the adiabatic constant.

Yabe et al. (2001) extended this equation to multiphase flow simulations by introducing a color function into the convection equation， which are shown as follows:

$$\frac{\partial \alpha}{\partial t}+u_i\frac{\partial \alpha}{\partial x_i}=0 \tag{2a}$$

$$\frac{\partial \rho}{\partial t}+u_i\frac{\partial \rho}{\partial x_i}=-\rho\frac{\partial u_i}{\partial x_i} \tag{2b}$$

$$\frac{\partial u_i}{\partial t}+u_j\frac{\partial u_i}{\partial x_i}=\frac{1}{\rho}\frac{\partial \tau_{ij}}{\partial x_j}-\frac{1}{\rho}\frac{\partial p}{\partial x_i}+f_i \tag{2c}$$

$$\frac{\partial p}{\partial t}+u_i\frac{\partial p}{\partial x_i}=-\rho C_S^2\frac{\partial u_i}{\partial x_i} \tag{2d}$$

where τ_{ij} is the viscous part of the stress tensor of the Newtonian fluid. f_i is the external force. μ is the fluid viscosity. C_S is the speed of sound in the mixture. α is the volume fraction of gas or liquid.

Based on the assumptions that the water phase is incompressible and dominates the fluid motion, and that the gas density just depends on pressure, Wei et al.(2021) simplified the governing equations for two-phase water-air flow. They proposed a set of pressure-based governing equations for compressible gas and incompressible liquid two-phase flow, which takes the following form:

$$\frac{\partial \alpha_g}{\partial t}+u_i\frac{\partial \alpha_g}{\partial x_i}=\left(1-\alpha_g\right)\frac{\partial u_i}{\partial x_i} \tag{3a}$$

$$\frac{\partial \rho u_i}{\partial t} + u_j \frac{\partial \rho u_i}{\partial x_j} = \frac{\partial \tau_{ij}}{\partial x_j} - \frac{\partial p}{\partial x_i} + f_i \tag{3b}$$

$$\frac{\partial p}{\partial t} + u_i \frac{\partial p}{\partial x_i} = -C_g^2 \frac{\tilde{\rho}_g}{\alpha_g} \frac{\partial u_i}{\partial x_i} \tag{3c}$$

where α_g is the volume fraction of the gas phase. ρ_g is the gas phase density. C_g is the speed of sound in the gas.

The simplified governing equations differ from the equation (2) primarily in the following aspects: (i) In equation (2), density and pressure are related through the equation of state (EOS), and separate solutions for both the density and pressure equations are required. In contrast, equation (3) employs pressure p as one of the primary variables, with density being determined through the EOS. This eliminates the need for a separate density equation, while maintaining the discontinuity of density at the water-air interface, thus improving the accuracy of density calculations. (ii) In equation (2), the source term on the right-hand side of the pressure equation involves a water-air mixture variable. The improved model retains only the variables related to the gas phase, while the water phase is treated as incompressible instead of weakly compressible, thereby avoiding the limitation of the time step imposed by the speed of sound in the water phase.

2.2 Wave Generation

To enhance the numerical stability of wave generation, a momentum source term is added to the governing equations to generate the target waves. The momentum source function (Choi and Yoon, 2009) is given by:

x direction:

$$s_x^m = g\left(2\beta x\right)\exp\left(-\beta x^2\right)\frac{1}{4\pi^2}\int_{-\infty}^{\infty}\int_{-\infty}^{\infty}\frac{iD\left(k_y,\omega\right)}{\omega}\exp\left[i\left(k_y y-\omega t\right)\right]d\omega dk_y \tag{4}$$

y direction:

$$s_y^m = g\exp\left(-\beta x^2\right)\frac{1}{4\pi^2}\int_{-\infty}^{\infty}\int_{-\infty}^{\infty}\frac{k_y D\left(k_y,\omega\right)}{\omega}\exp\left[i\left(k_y y-\omega t\right)\right]d\omega dk_y \tag{5}$$

where h is the water depth, D is the source function amplitude, $D=\dfrac{H\left(\omega^2-\alpha_1 g k^4 h^3\right)\cos\theta}{\omega I_1 k\left[1-\alpha\left(kh\right)^2\right]}$, $I_1=\sqrt{\dfrac{\pi}{\beta}}\exp\left(-\dfrac{k^2}{4\beta}\right)$, $\alpha_1=\alpha+\dfrac{1}{3}$, $\alpha=\dfrac{z_\alpha}{h}\left(\dfrac{1}{2}\dfrac{z_\alpha}{h}+1\right)$, $z_\alpha=-0.53h$, β is the parameter associated with the width of source function, $\beta=\dfrac{80}{\delta^2 L^2}$, $\delta=2W/L$ is a relevant parameter for the width of wave making region, W is the width of source region. ω,k,θ,H,L are the wave parameters of angular frequency, wave number, wave direction, wave height and wave length, respectively.

For two-dimensional linear monochromatic regular waves, the momentum source function can be simplified as follows:

$$s^m = -g\left(2\beta x\right)\exp\left(-\beta x^2\right)\frac{D}{\omega}\sin\left(-\omega t\right) \tag{6}$$

2.3 Computational Domain and Boundary Conditions

The layout of the two-dimensional numerical wave flume used in this study is shown in Figure 1. The origin of the coordinate system is located at the intersection of the centerline of the wave generation zone and the still water level. The width of the wave generation zone is set to be equal to the target wavelength, while the wave absorption zones at both ends of the flume are each set to be twice the wavelength in width. To mitigate the effects of reflected waves, a sponge layer absorption method is employed. The absorbing coefficient is determined using the method proposed by Wei et al. (1995),

$$A_b = c_\alpha \frac{\exp\left[\left(\left(\frac{|x-x_0|}{x_l}\right)^n\right]-1}{\exp(1)-1} \tag{7}$$

where x_0 is the starting position of the wave absorption zone, x_l is the length of the wave absorption zone, c_α and n are the damping coefficients determined via the numerical test. Following the conclusions of Lin et al. (2004), $c_\alpha = 200$, $n_c = 10$. The other boundaries of the flume are assigned no-slip boundary conditions.

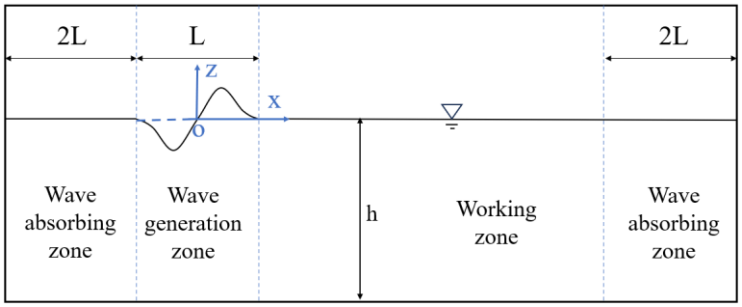

Fig.1 Sketch of the numerical wave flume

2.4 Numerical scheme

The governing equations are solved using the fractional step approach(Chorin, 1968). The computation process from time n to n+1 is divided into three steps.

(1) Advection phase

$$\frac{\alpha_g^* - \alpha_g^n}{\Delta t} + u_i^n \frac{\partial \alpha_g^n}{\partial x_i} = 0 \tag{8}$$

$$\frac{u_i^* - u_i^n}{\Delta t} + u_j^n \frac{\partial u_i^n}{\partial x_j} = 0 \tag{9}$$

$$\frac{p^* - p^n}{\Delta t} + u_i^n \frac{\partial p^n}{\partial x_i} = 0 \tag{10}$$

The intermediate solution α^* is obtained by solving Equation (8) using the THINC/WLIC scheme, while the intermediate solutions u_i^* and p^* are computed by solving Equations (9) and (10) using the WENO scheme.

(2) Non-advection phase(i)

$$\frac{u_i^{**} - u_i^*}{\Delta t} = \frac{1}{\rho^*}\frac{\partial}{\partial x_i}\left(2\mu^* S_{ij}^* - \frac{2}{3}\mu^* \delta_{ij} S_{kk}^*\right) + g_i + s_i^m + A_b u_i^* \tag{11}$$

The intermediate solution u_i^{**} is obtained by solving Equation (11) using the central difference method.

(3) Non-advection phase(ii)

$$\frac{\alpha_g^{n+1} - \alpha_g^*}{\Delta t} = \left(1 - \alpha_g^*\right)\frac{\partial u_i^{n+1}}{\partial x_i} \tag{12}$$

$$\frac{u_i^{n+1} - u_i^{**}}{\Delta t} = -\frac{1}{\rho^*}\frac{\partial p^{n+1}}{\partial x_i} \tag{13}$$

$$\frac{p^{n+1} - p^*}{\Delta t} = -C_g^2 \frac{\tilde{\rho}_g^*}{\alpha_g^*}\frac{\partial u_i^{n+1}}{\partial x_i} \tag{14}$$

The divergence of Equation (12) is computed, and together with Equation (13), this yields the pressure Poisson equation,

$$\frac{\alpha_g^*\left(p^{n+1}-p^*\right)}{C_g^2\tilde{\rho}_g^*\Delta t^2}+\frac{1}{\Delta t}\frac{\partial u_i^{**}}{\partial x_i}=\frac{\partial}{\partial x_i}\left(\frac{1}{\rho^*}\frac{\partial p^{n+1}}{\partial x_i}\right) \tag{15}$$

p^{n+1} is obtained by solving Equation (14), which is then substituted into Equation (12) to compute u_i^{n+1}. Finally, α^{n+1} is determined using Equation (11). This completes the numerical solution for one time step. During the computation, the time step is updated according to the CFL.

3.MODEL VALIDATION

In this simulation, the still water depth h is 0.2 m, the flume length is 13.3 m, the wave period T is 1.0 s, and the wave height H is 0.01 m. The wave generation zone is centered at $x = 0$ m, and the width of the momentum source zone is equal to the wavelength in the x-direction. The wave absorption zones are located at both ends of the flume. The grid spacing is set to $\Delta x = 1.0$ cm and $\Delta y = 0.05$ cm, with a total simulation time of 18 s. The CFL number is chosen to be 0.25.

Figure 2 presents the time history of the wave surface at locations 2, 4, and 6 wavelengths away from the center of wave generation zone. The wave heights and periods at the measurement points, as obtained from the model, match the analytical solutions.

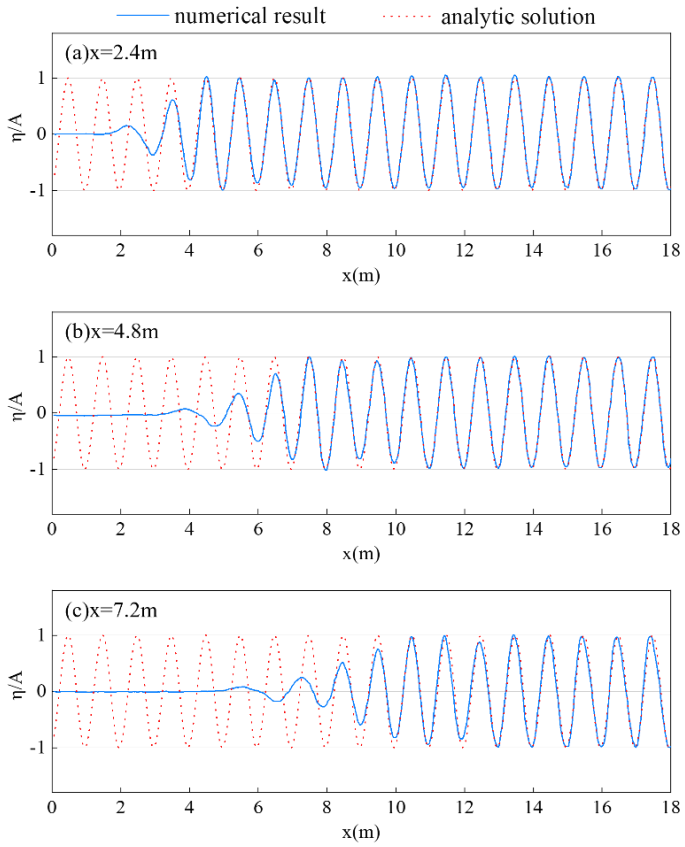

Fig.2 Time history of wave profiles at each measurement point

4.SIMULATION OF WAVE IMPACT ON A HORIZONTAL PLATE

The wave impact on a horizontal plate involves complex fluid-structure interactions and air-water dynamics, making it one of the key research topics in the field of marine engineering. A numerical wave model, as shown in Figure 3, is developed based on the physical model experiments of Ren et al. (2019) to simulate and analyze the influence of gas on the wave impact pressure acting on a horizontal plate. The numerical wave tank has a length of 20.4 m, a water depth of 0.35 m, and the horizontal plate is 1.2 m long and 0.006 m thick. The plate is positioned 3 wavelengths away from the wave generation boundary on the left side, and is placed at the still water level. Twenty-four wave measurement points are evenly spaced at 5 cm intervals along the bottom of the plate, with the first point (P1) located 2.5 cm

from the left edge of the plate. The incident wave has a wavelength of 2.4 m and a wave height of 0.08 m. The model is configured with grid spacings of $\Delta y = 1.0$ cm, $\Delta y = 0.25$ cm and a CFL number of 0.5.

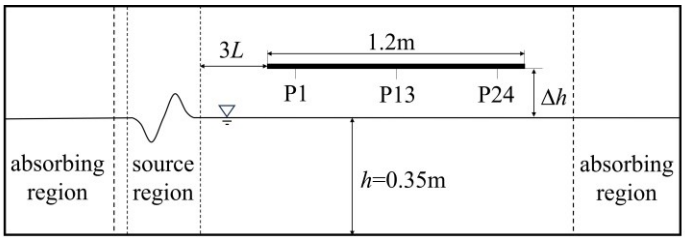

Fig.3 Sketch of numerical wave flume for wave impact horizontal plate

Figure 4 shows a comparison between the impact pressure-time histories obtained from the present numerical model at three locations: the front end (P1), middle section (P13), and rear end (P24), and the experimental data from Ren et al. (2019). As illustrated, the simulation results from the numerical model exhibit a good overall agreement with the experimental measurements. The period, amplitude, and time-dependent characteristics of the impact pressure are in close alignment with the observed data. Additionally, the numerical results from this study successfully capture the pressure oscillations caused by the compressibility of air.

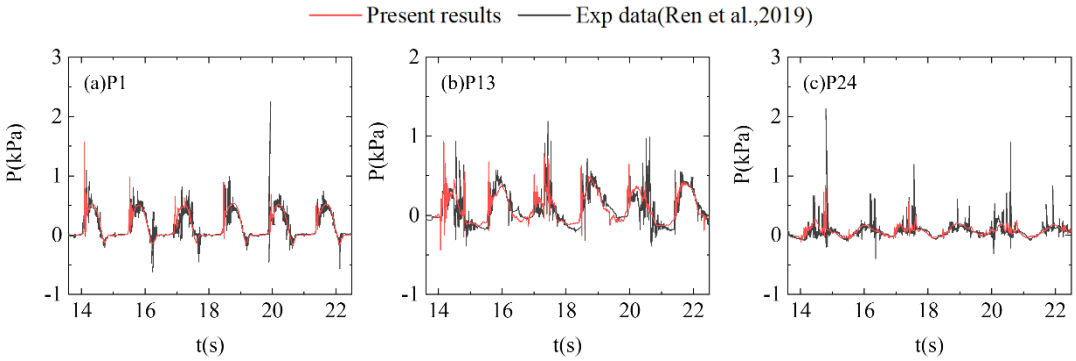

Fig.4 Pressure variation at the bottom of the horizontal plate

Previous studies have demonstrated that air entrapment and the compressibility of air have significant effects on breaking wave loads (Bullock et al., 2007; Bredmose et al., 2009; Liu et al., 2019; Sun et al., 2019). Building upon the physical experiments conducted by Ren et al. (2019), this study increases the width of the flat plate to capture multiple air pockets at the bottom of the plate. The arrangement of the numerical wave tank is consistent with that shown in Figure 5, and the wave conditions are the same as those in the experiments. However, the relative wavelength (L/B) is set to 1(Case 1) and 0.5(Case 2), respectively. The effect of the number and distribution of air pockets on wave pressure loads is then investigated.

Figure 5 illustrates the synchronized air pocket-pressure data over one wave period under different relative wavelength conditions. The moment when the free surface first contacts the front end of the plate within a wave period is defined as t = 0.00 s. At this time, in Case 1, two enclosed air pockets are formed at the front and rear ends of the plate, with the maximum impact pressure occurring at the front of the plate. In Case 2, the air beneath the flat plate is divided into two distinct regions: a larger air cavity forms at the front and middle of the plate, while the air at the rear is connected to the atmosphere.

As the wave propagates forward, at t = 0.35 s, in Case 1, the front air pocket moves toward the rear of the plate, leading to an increase in pressure within the pocket, while the rear air pocket overflows from the back of the plate, causing the rear of the plate to connect with the atmosphere and the pressure to approach atmospheric pressure. In Case 2, due to the rising water surface, three air pockets form beneath the plate, with the highest pressure occurring in the first air pocket. In each air pocket, the largest pressure occurs at the front, where the water directly contacts the underside of the plate.

At t = 0.65 s, the water at the front of the plate begins to recede, causing the pressure to decrease and even become negative. In Case 1, at the rear of the plate, water rises and contacts the plate, increasing

the pressure. In Case 2, the three air pockets move toward the rear. Compared to the previous time step, the pressure within the air cavity decreases.

At t = 1.25 s, the water at the front of the plate has separated from the plate's bottom, and the pressure returns to atmospheric pressure. In Case 1, the air pocket moves to the rear of the plate, where the pressure is the highest across the entire plate. In Case 2, as the water surface falls, the air pockets merge, and the rear air pocket overflows from the back of the plate, connecting with the atmosphere. As the regular wave continues to propagate, at t = 1.45 s, the wave surface once again makes contact with the front end of the plate.

Throughout the entire wave impact process, the pressure distribution within the air pockets remains relatively uniform. Furthermore, the presence of multiple air pockets may extend the range of impact pressure effects along the bottom of the plate, thereby increasing both the magnitude of the total force and its duration.

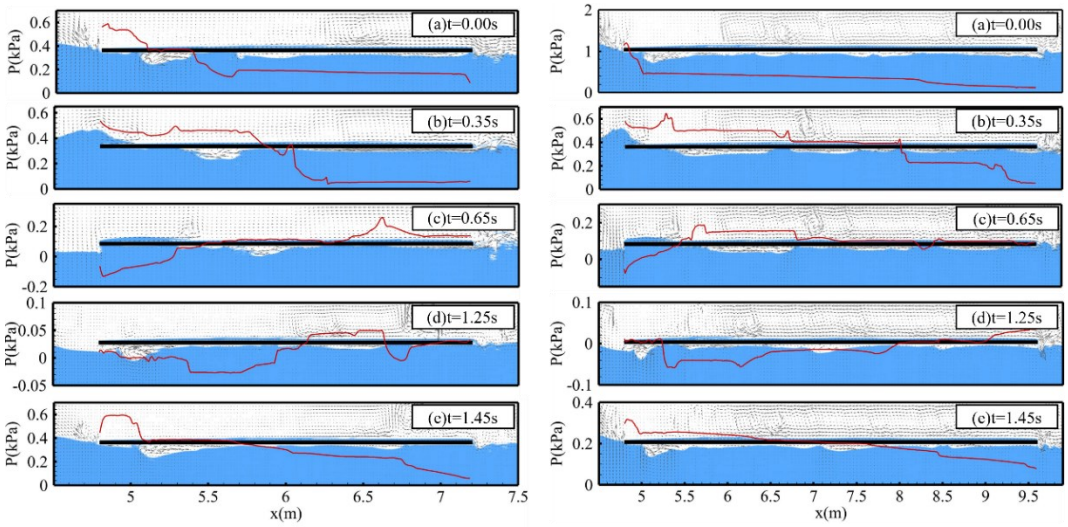

(a)Case1:L/B=1.0 **(b)Case2:L/B=0.5**

Fig.5 The distribution of air pockets and pressure values at the bottom of the plate

Seventeen measurement points are evenly distributed along the bottom of the plate. The measurement points are numbered sequentially from the front 1 to the rear 17 of the horizontal plate. The impulsive forces at each point over one wave cycle were calculated. The results for Case 1 and Case 2 are shown in the figure 6. It can be observed that the impulsive forces at both ends of the plate are similar in magnitude for both cases, while a significant difference is evident in the middle of the plate. Specifically, for the case with Case2, the impulsive force in the middle is consistently higher than that for Case1. The observed phenomenon is hypothesized to result from the greater number of closed cavitation bubbles that form at the bottom of the plate in Case 2. These cavitation bubbles contribute significantly to the overall lift force, which in turn leads to a larger impulsive force in the middle region of the plate.

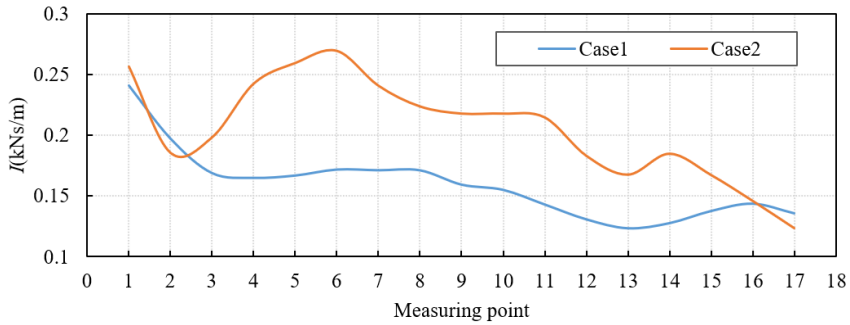

Fig.6 The impulsive force at different measurement points over a single wave period

CONCLUSIONS

This study develops a numerical wave model based on an improved compressible and incompressible gas-liquid governing equation. The model is applied to simulate and analyze the wave impact on a horizontal plate.

The regular wave generated by the model shows good agreement with analytical solutions, indicating that the model demonstrates high accuracy in numerical wave generation and wave propagation simulation.

Simulation results of wave impact on the horizontal plate suggest that the model produces impact pressure profiles that are in good agreement with experimental data. By incorporating the compressibility of air, the model proves to be highly suitable for simulating wave impact problems. Further analysis of wave impact on the plate under different relative wavelength conditions reveals that the number and distribution of air pockets significantly influence the pressure load on the bottom of the plate.

REFERENCES

AJ Chorin. 1968. Numerical solution of the Navier-Stokes equations. *Mathematics of Computation* , 22, 745–762.

Beji, S., Battjes, J.A. 1993. Experimental investigation of wave propagation over a bar. *Coastal Engineering* ,19, 151–162.

Bredmose, H., Peregrine, D.H., Bullock, G.N. 2009. Violent breaking wave impacts. Part 2: Modelling the effect of air. *Journal of Fluid Mechanics*, 641, 389–430.

Bullock, G.N., Obhrai, C., Peregrine, D.H., Bredmose, H. 2007. Violent breaking wave impacts. Part 1: Results from large-scale regular wave tests on vertical and sloping walls. *Coastal Engineering*, 54, 602–617.

Chang, K.-A., Ariyarathne, K., Mercier, R. 2011. Three-dimensional green water velocity on a model structure. *Experiments in Fluids*, 51, 327–345.

Choi, J., Yoon, S.B. 2009. Numerical simulations using momentum source wave-maker applied to RANS equation model. *Coastal Engineering*, 56, 1043–1060.

Duong, T.T., Jung, K.H., Lee, G.N., Park, H.J., Lee, J., Suh, S.B., 2021. Experimental study on wave-in-deck loading under focused wave conditions. *Ocean Engineering*, 242, 110146.

E., D., D.R.C.B., N., R., M., M.G., N. 2014. Wave interaction with a vertical wall: SPH numerical and experimental modeling. *Ocean Engineering*, 88, 330–341.

Ghalandari, M., Bornassi, S., Shamshirband, S., Mosavi, A., Chau, K.W. 2019. Investigation of submerged structures' flexibility on sloshing frequency using a boundary element method and finite element analysis. *Engineering Applications of Computational Fluid Mechanics*, 13, 519–528.

Hu, Z.Z., Greaves, D., Raby, A. 2016. Numerical wave tank study of extreme waves and wave-structure interaction using OpenFoam®. *Ocean Engineering*, 126, 329–342.

Lin, P., Liu, P.L.-F. 2004. Discussion of "vertical variation of the flow across the surf zone" [coast. Eng. 45 (2002) 169–198]. *Coastal Engineering*, 50, 161–164.

Liu, S., Gatin, I., Obhrai, C., Ong, M.C., Jasak, H. 2019. CFD simulations of violent breaking wave impacts on a vertical wall using a two-phase compressible solver. *Coastal Engineering*, 154, 103564.

Liu, X.-D., Osher, S., Chan, T. 1994. Weighted essentially non-oscillatory schemes. *Journal of Computational Physics,* 115, 200–212.

Ma, L., Swan, C. 2020. An experimental study of wave-in-deck loading and its dependence on the properties of the incident waves. *Journal of Fluids and Structures,* 92, 102784.

Ma, Z., Zhou, T., Ren, N., Zhai, G. 2019. A comprehensive study of the wave impact loads on an inclined plate. *Journal of Marine Science and Engineering*, 7, 103.

Ren, X., Sun, Z., Liang, S. 2019. Probability analysis of impact pressures of regular waves on a 2D horizontal plate. *The Ocean Engineering*, 37, 1–11.

Ryu, Y., Chang, K.-A., Lim, H.-J. 2005. Use of bubble image velocimetry for measurement of plunging wave impinging on structure and associated greenwater. *Measurement Science and Technology*, 16, 1945–1953.

Ryu, Y., Chang, K.-A., Mercier, R. 2007. Runup and green water velocities due to breaking wave impinging and overtopping. *Experiments in Fluids*, 43, 555–567.

Salih, S.Q., Aldlemy, M.S., Rasani, M.R., Ariffin, A.K., Ya, T.M.Y.S.T., Al-Ansari, N., Yaseen, Z.M., Chau, K.-W. 2019. Thin and sharp edges bodies-fluid interaction simulation using cut-cell immersed boundary method. *Engineering Applications of Computational Fluid Mechanics*, 13, 860–877.

Sun, H., Sun, Z., Liang, S., Zhao, X. 2019. Numerical study of air compressibility effects in breaking wave impacts using a CIP-based model. *Ocean Engineering*, 174, 159–168.
Wei, G., Kirby, J.T. 1995. Time-dependent numerical code for extended boussinesq equations. *Journal of Waterway, Port, Coastal, and Ocean Engineering*, 121, 251–261.
Wei, Z., Jiang, Q., Nie, S. 2021. A pressure-based numerical scheme for compressible–incompressible two-phase flows. *Numerical Methods in Fluids*, 93, 3215–3230.
Yabe, T., Wang, P.-Y. 1991. Unified numerical procedure for compressibleand incompressible fluid. *Journal of the Physical Society of Japan*, 60, 2105–2108.
Yabe, T., Xiao, F., Utsumi, T. 2001. The constrained interpolation profile method for multiphase analysis. *Journal of Computational Physics*, 169, 556–593.
Yokoi, K. 2007. Efficient implementation of THINC scheme: A simple and practical smoothed VOF algorithm. *Journal of Computational Physics*, 226, 1985–2002.
Zhai, G., Zhou, T., Ma, Z., Ren, N., Chen, J., Teh, H. 2021. Comparison of impulsive wave forces on a semi-submerged platform deck, with and without columns and considering air compressibility effects, under regular wave actions. *Engineering Applications of Computational Fluid Mechanics*, 15, 1932–1953.
Zhao, X., Hu, C., Sun, Z. 2010. Numerical simulation of extreme wave generation using VOF method. *Journal of Hydrodynamics*, 22, 466–477.